ISBN 978-82-326-3504-7 (printed version)
ISBN 978-82-326-3505-4 (electronic version)
ISSN 1503-8181

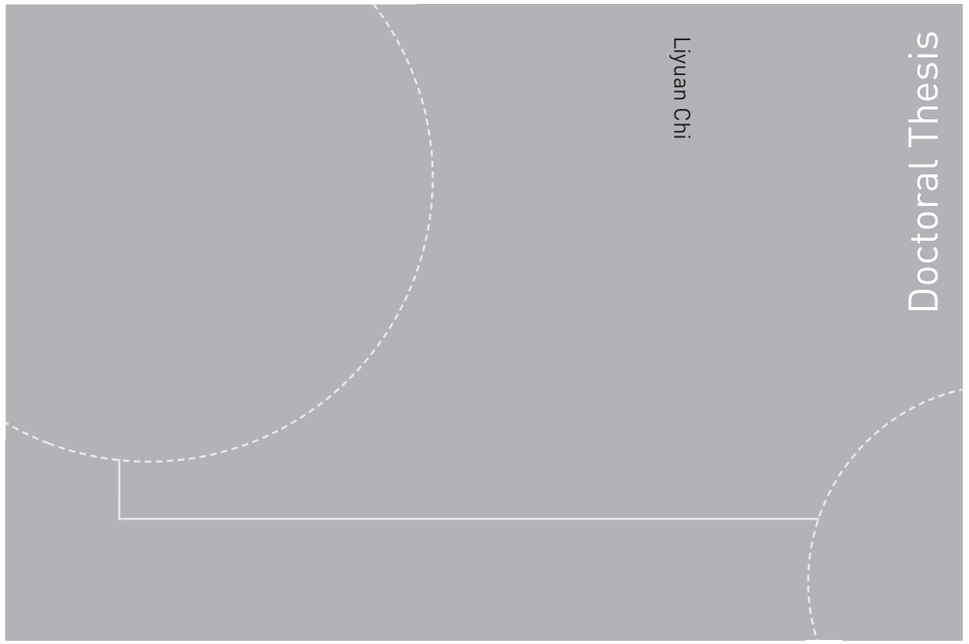

Doctoral theses at NTNU, 2018:358

Liyuan Chi

Shock compression and fractures in laboratory rock blasting

NTNU
Norwegian University of
Science and Technology
Faculty of Engineering
Department of Geoscience and Petroleum

NTNU
Norwegian University of
Science and Technology

UNIS
The University Centre in Svalbard

Doctoral theses at NTNU, 2018:358

NTNU
Norwegian University of
Science and Technology

Liyuan Chi

Shock compression and fractures in laboratory rock blasting

Thesis for the degree of Philosophiae Doctor

Trondheim, November 2018

Norwegian University of Science and Technology
Faculty of Engineering
Department of Geoscience and Petroleum

NTNU
Norwegian University of Science and Technology

UNIS
The University Centre in Svalbard

NTNU
Norwegian University of Science and Technology

Thesis for the degree of Philosophiae Doctor

Faculty of Engineering
Department of Geoscience and Petroleum

ISBN 978-82-326-3504-7 (printed version
ISBN 978-82-326-3505-4 (electronic version
ISSN 1503-8181

Doctoral theses at NTNU, 2018:358

Printed by Skipnes Kommunikasjon as

Preface

This doctoral thesis has been submitted to the Norwegian University of Science and Technology (NTNU) for the degree of *Philosophiae Doctor* (PhD). The research was carried out at the Department of Arctic Technology, the University Centre in Svalbard (UNIS) in Longyearbyen, Norway. The work was mainly financed by UNIS, and partially financed by NTNU.

Professor Zong-Xian Zhang (The University Centre in Svalbard/University of Oulu 2017), Professor Charlie Chunlin Li (NTNU) and Professor Arne Aalberg (The University Centre in Svalbard/NTNU) have supervised the PhD work. The thesis consists of three parts. Each part mainly comprises a journal paper. Two additional conference papers complement the journal papers. The author has been responsible for planning and performing all experimental tests. Furthermore, the author analyzed and interpreted the experimental data, produced all figures, and wrote the journal and conference papers. The supervisors, who were co-authors for all papers, have contributed with guidance and supervision of the PhD work and reviewing the manuscripts. The experiments were conducted in collaboration with Professor Jun Yang from the Beijing Institute of Technology, with the assistance of master students and PhD candidates.

Liyuan Chi,

Longyearbyen, Norway

6 September 2018

Acknowledgements

I would like to express my gratitude towards my supervisors Professor Zong-Xian Zhang, Professor Arne Aalberg, and Professor Charlie Chunlin Li. They have provided me with support and invaluable feedback on my work.

I am grateful to Professor Jun Yang for his kind assistance in the use of the explosion facility for blast tests and for valuable advice on the tests. Associate professor Helena Reinardy and Dr. Graham Gilbert are thanked for valuable inputs to manuscripts of Paper I and Paper III, respectively. I would like to thank Dr. Chenglong He for the assistance with static and dynamic strength testing on granite and for sharing a report of heavy mineral analysis for granite he ordered.

The following students from the Beijing Institute of Technology are acknowledged for their assistance to the experimental work: Zhanyang Chen, Zongshan Zou, Hongliang Tang, and Di Zhang. A further thank you to my colleges at the department at UNIS for making these four years very enjoyable, both on and off work.

Finally, I would like to thank family and friends that have supported me through these four years.

This thesis is dedicated to my dear parents.

Abstract

Rock blasting is one of the most important operations in hard rock engineering work, especially in mining and tunneling. Current rock blasting practices are primarily based on empirical designs, and mechanisms of rock fracture by blasting are not clear. An improved and scientifically based blast design depends on a better understanding of the fundamentals of rock blasting, which include detonation physics, shock-wave characteristics, rock fracturing and fragment movements. This PhD thesis mainly investigates the shock compression of rock in the vicinity of an exploding charge and rock fracturing on a free surface parallel to the blasthole.

Small-scale blast tests were carried out with granite cylinders and cubes. The tests were divided into three parts, which correspond to three separate but closely connected topics of the thesis. The logical order for the three parts is based on the distance to explosive charges; starting from the vicinity of charges to the free surface of the specimens.

Part 1 focused on the pressure and attenuation of shock waves in granite. Ten test granite cylinders were subjected to explosion from pressed trinitrotoluene (TNT) charges placed centrically in the specimens. Three cylinders had dimensions Ø150 mm × 200 mm; seven had dimensions Ø240 mm × 300 mm. All the specimens had concentric holes drilled from both ends: one 20-mm hole to place the explosive charge and one 50-mm hole to insert a granite plug equipped with Manganin gauges, which measured the pressure of shock waves. One or two gauges were used in each inserted cylinder at distances 7, 15, 22 or 35 mm from the explosive charge in the axis direction of cylinders. As the detonation-type explosion occurred, the measurement results indicated that the peak pressure varied from 4.4 GPa to 15.9 GPa depending on the distance from the explosive, with pressure rise time of ~0.5 μs. An exponential relation between the peak shock pressure and the distance was found on the basis of the measurement results with an attenuation factor of 0.04. For specimens with two gauges, shock-wave velocities in granite various distances from the explosive ranged from 4.58 mm μs^{-1} to 5.34 mm μs^{-1}. As the deflagration-type explosion occurred, the measured peak pressure was 1.35 GPa 11 mm from the charge, with a 16 μs pressure rise time.

Part 2 included nine blast tests on granite cylinders with a diameter of either 228 mm or 240 mm and a length of 300 mm, with fully coupled or decoupled explosive charges. The granite cylinders were confined by steel tubes with an inside diameter of 268 mm. The gap between was left either empty, filled with gravel or filled with cement grout. This was implemented to simulate free, semi-confined or fully confined boundary conditions, respectively. The fractures around the blast hole were examined on the cross-sections of the cylinders. For the specimens with fully confined boundary, the diameter of the expanded borehole from a fully coupled charge was up to 2.37 times the initial borehole diameter, and the value at the decoupling ratio of 1.75 was approximately 1.1 times the initial diameter. The size of the crushed zone for the same specimens (decoupling ratio is 1.75) was 1.32~1.56 times the initial diameter. As the decoupling

ratio was 3.5, the borehole expansion and the crushed zone were not observed. Combining with other studies, the results indicated that the borehole expansion and the crushed zone depended on the decoupling ratio, the properties of the explosive (such as the density and the VOD), and the given confinement. For small-weight charges, the cylinders confined by gravel fill developed more radial cracks than those observed in the cylinders confined by cement fill. The length and opening of the cracks were also larger in the gravel-fill cylinders. For large-weight charges, a cylinder with empty gap was fragmented into very small pieces, while a cylinder with cement fill was broken into large fragments. Hoop strains measured on the steel tubes were smaller for a specimen with gravel fill than for a similar one with cement fill. For a cylinder with empty gap, fragment collisions with the steel tube caused significant hoop strains in the confining steel tube.

Part 3 dealt with six blast tests with granite cubes ($400 \times 400 \times 400$ mm^3) using a combination of data collected from strain gauges and generated by digital image correlation (DIC) analysis of pictures captured using a high-speed camera. The maximum concentration of strain obtained from the DIC analysis corresponded well to the dominant cracks and fracture patterns observed on the specimens. By combining the results from the strain gauges and the results from the DIC analysis, the dominant cracks observed on the front surface were found to initiate from or around the surface rather than from the cracks radiating from the borehole. For the fracture pattern on the monitored specimen surface, the increase in charge length primarily influenced the number of dominant vertical cracks, rather than the number of dominant horizontal cracks. From the image analysis, charge weights markedly affected the initiation time for macroscopic cracks and the gas ejection time. By tracing the in-plane motion of corner fragments, it was found that the translational velocities were directed mainly transversely to the charge axis and that the velocity magnitudes were influenced by charge weights.

The experimental findings of this investigation may contribute to a better understanding of the fundamental mechanisms of the rock fracture by blasting. It may also be useful to verify numerical models that simulate the blasting process.

List of Papers

The main part of the thesis consists of the following papers.

Journal papers:

Paper I.

Chi LY, Zhang ZX, Aalberg A, Yang J, Li. CC, Measurement of shock pressure and shock-wave attenuation near a blast hole in rock. Int J of Impact Eng (2018). Under review after revision.

Paper II.

Chi LY, Zhang ZX, Aalberg A, Li. CC, Experimental investigation of blast-induced fractures in rock cylinders. Rock Mech Rock Eng. Under review.

Paper III.

Chi LY, Zhang ZX, Aalberg A, Yang J, Li. CC, Fracture processes in granite blocks under blast loading. Rock Mech Rock Eng (2018). Accepted.

Conference papers:

Conference paper I

Chi LY, Zhang ZX, Aalberg A, Yang J (2018) An experimental investigation of fracture patterns near a blasthole in cylinders of granite under different radial confinements. In: Schunnesson H, Johansson D (eds) 12th International Symposium on Rock Fragmentation by Blasting. Luleå University of Technology, Luleå, Sweden, pp 85–92

Conference paper II

Chi L, Aalberg A, Zhang ZX, et al (2018) An experimental investigation on dynamic responses of granite blocks under blast loading. In: Li C, Li X, Zhang Z (eds) Proceedings of the 3rd international conference on rock dynamic and applications. Taylor & Francis Group, Trondheim, pp 623–628

Declaration of authorship

The author of this thesis, Liyuan Chi, planned, prepared and performed all the laboratory experiments, analyzed the results, and wrote the major part of the papers included in the thesis. The co-authors of the papers contributed in planning the experiments, discussions and evaluations of the results, and assisted in writing the papers.

Table of contents

PART I – Introduction to the doctoral thesis

PART II – Appended journal papers

PART I

Introduction to the doctoral thesis

1. Introduction

1.1. Background and motivation

Rock blasting is extremely important in hard rock mining and other rock engineering works. However, up till now rock blasting has been dominated by empirical design, which may result in considerable mineral loss, strong ground vibration, safety risks and the inefficient use of explosives (Zhang 2016). In production blasts, a blast plan usually includes arrangements of boreholes, charge parameters, primer placement and delay time in each borehole. In order to make a more efficient and reliable blast plan, there is a need for improved knowledge of rock fractures under blast loading.

Rock blasting in mining applications usually consists of a few to the order of a hundred boreholes per blast. In general, the blasted rock mass experiences a very complicated loading and unloading process, which leads to rock blasting being a complex issue. In detail, the detonating explosive in each borehole imparts a high transient pressure on the wall of the borehole, which generates a shock wave propagating into the rock mass. The effective loading at a point therefore depends on four main factors; the shock wave transmission and reflection at the explosive-to-rock interface at the individual boreholes, the outward shock wave attenuating to a stress wave through the rock, the interaction with stress waves from the neighbor boreholes, and the stress wave reflection from the rock mass boundaries. The rock mass in blasting experiences stresses at different levels of strain rate including quasi-static, dynamic and shock strain rate conditions (Meyers 1994; Hustrulid 1999).

To investigate and clarify the complex issue, the first step of research usually involves the examination of a single borehole blasting. According to the characteristics of the fractures in the rock surrounding a blasthole, the rock damage region is divided into different damage zones. Various notations and definitions of these zones have been used among scholars. In general, the blast-induced damage zones include a borehole expansion, a crushed zone and a fractured zone (Johansson and Persson 1970; Zhang 2016).

In the immediate vicinity of an exploding charge, the local rock bounded by a confining rock mass experiences a shock wave, where the shear stress and distortion of the rock can be neglected (Wang 2011). Here the rock is intensely crushed and shattered (Kutter and Fairhurst 1971). Most of the fines generated in rock blasting originate from this region (Kanchibotla et al. 1999). Cunningham et al. (2006) and Zhang (2016) defined the region between the circumference of the initial borehole and the circumference of the post-blast borehole as the borehole expansion zone. The annular region outside the expanded borehole, where the rock was crushed and shattered, was defined as the crushed zone. A similar definition is chosen in this thesis, as shown by Fig. 1.1. The original borehole is expanded to a post-blast borehole which has an uneven periphery, and is surrounded by a crushed zone where the rock has developed a dense

radial and circumferential cracked region. The fractured zone outside the crushed zone contains mainly radial cracks, which are mostly initiated by the tangential component of the stress waves (Saharan et al. 2006; Lu et al. 2016; Zhang 2016). Coarser rock fragments in blasting are generated in this zone (Kanchibotla et al. 1999).

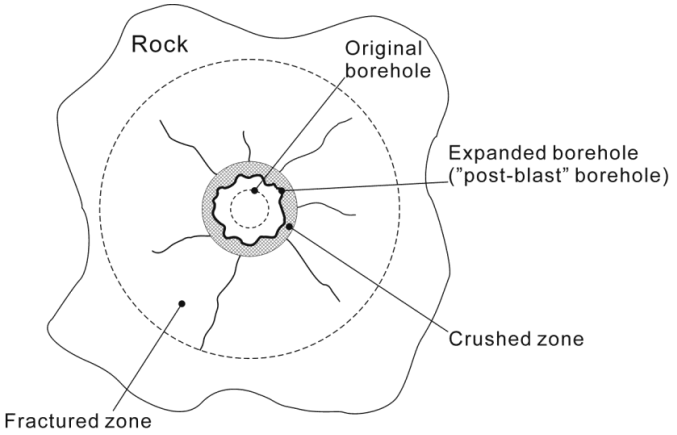

Figure 1.1 Definitions of damage zones around a borehole

Boundary conditions of rock strongly influence fracture formation within the fractured zone. A free surface favors the generation of fractures as wave reflections on the surface bring about tensile stress waves (Field and Ladegaard-Pedersen 1971; Kutter and Fairhurst 1971). This is considering that spalling will happen near the free surface when the magnitude of the reflected wave is greater than the dynamic tensile strength of the rock (Rossmanith and Uenishi 2006; Wang 2011; Zhang 2016). In addition, the interaction between reflected waves and outwardly travelling radial cracks leads to a fracture network in fractured zone (Fourney 2015). Rock fragmentation thus occurs.

Rock blasting has been studied by many scholars, with the majority paying attention to fractures in the fractured zone, i.e., radial crack initiation and propagation, or fragment size distributions from rock fragmentation. Most uncertainties and deficiencies in the understanding of rock blasting are likely connected to the response of the rock in the near field of the borehole, in particular the shock compression of the rock materials surrounding the borehole. The shock response in the near field highly influences the stress waves and the fractures in the fractured zone.

1.2. Objectives

The overall aim of the research presented in this thesis was to understand the mechanism of rock fracture by blasting, focusing on shock compression in the near field and rock fracturing on the free surface. Specific objectives were defined as follows:

- To investigate the shock wave propagation in the vicinity of blastholes.
- To investigate the blast-induced fractures around blastholes in rock.
- To investigate the fracturing of the free surface parallel to blastholes in rock.
- To collect data, both deformations and crack initiation on the free surface.

The thesis presents the results in the appended journal papers in detail.

1.3. Research methodology

To reach the objectives, a common research methodology was employed for all the different parts of the thesis. Due to the complexity of rock blasting and numerical simulation with limited accuracy, a laboratory scale experimental investigation is important and necessary for studying fractures caused by an exploding charge. A series of single-hole blast tests were designed, paying special attention to data collection during blasting. This simplified the subsequent analysis of the measured results. The tests were performed with granite cylinders and cubes under highly controlled conditions. In the tests on the cylinders, shock pressures in the vicinity of the blastholes were measured using embedded pressure gauges along the axis direction of the cylinders, whereas deformation on the surfaces of the cubic specimens were measured by means of digital image correlation (DIC) analysis and conventional strain gauge measurements. Fractures of some post-blast specimens were examined and compared to previously available data for additional findings. Replicate blast tests were conducted to increase the certainty of the experimental results. The mechanical properties of the granite were measured for interpreting the test results and later comparative studies and numerical models for blast simulation.

1.4. Research limitations

This thesis is limited to small-scale experiments, where the specimen material is medium-grained granite. The experiments focused on single-hole blasts, where the shock response of the rock was investigated along the axial direction of the exploding charge. Two main factors, the decoupling ratio and the boundary conditions, were taken into consideration, both influencing the blast-induced fractures. The thesis does not cover a complete analysis of fragment size distribution.

1.5. Outline of the thesis

This PhD thesis consists of three parts.

PART I consists of five chapters. Chapter 1 is an introduction to the research topic. Chapter 2 includes a wide range of literature reviews about monitoring blast tests and previous related investigations. Chapter 3 presents the experimental method to achieve the objectives listed in Section 1.2. Chapter 4 gives the main results by summing up the results of each paper. The final Chapter 5 comprises the conclusions and suggestions for further research.

PART II contains the three journal papers, which constitutes the main part of the thesis.

PART III contains two conference papers which complement the journal papers, including extra photos and specimen responses.

2. Literature review

Many scientists have worked on rock fractures by blasting by experimental investigations for several decades. Some of their studies are briefly explained in the following section. Here, the near field is defined by the outer boundary of the crushed zone.

2.1. Pressure measurement in blast tests

The magnitude of pressure is considered to be the essential parameter in detonation wave and shock wave characterization, even in the shock wave in a solid, while the material stresses would be the important parameter to characterize the stress wave. Since the 1980's, some scientists have attempted to measure borehole pressures occurring in blasting. From small-scale blast experiments, Fourney et al. (1981, 1983) measured the borehole pressure in methyl methacrylate (PMMA) blocks and found that the maximum pressure was on the order of magnitude of 10 MPa in highly decoupled blastholes. Nie (1999) developed a sensor with a carbon resistor gauge in a liquid and measured the borehole pressure developed in tests on large granite blocks. He found that the maximum pressure typically varied from 0.08 to 1.4 GPa. Mencacci and Chavez (2005) employed a measuring system based on a carbon resistor gauge enclosed in inert materials and determined the borehole pressure at the top of the explosive. The maximum pressure was found to be higher than 8 GPa in a fully-charged borehole with ammonium nitrate/fuel oil explosive (ANFO). Banadaki (2010) conducted blast experiments with granite cubic and cylindrical specimens with a small charge (approximately 0.18~0.8 g pentaerythritol tetranitrate (PETN)) and measured the pressure using carbon resistor gauges mounted in drilled holes 11~45 mm away from the borehole, and determined maximum pressures of approximately 70 MPa. Davies et al. (1997) used polyvinylidene fluoride (PVDF) gauges to measure the compressive stresses in polytetrafluoroethylene (PTFE) blocks inserted in boreholes and found maximum stresses in the range of 6.1 to 14.8 GPa. Taylor et al. (2009) used PVDF gauges mounted in limestone blocks and measured the compressive stresses, where the maximum stress was approximately 3.5 MPa at a distance of 200 mm away from the borehole.

For pressure measurements in blast tests, the pressure gauge selection is essential to achieve reliable results. Ginsberg and Asay (1991) noted that carbon resistor gauges had a better survivability than did Manganin gauges in some applications, and a low upper limit of measured pressures (up to 5 GPa). Rosenberg et al. (2007) performed plate impact experiments and found that carbon resistor gauges were not capable of capturing data for pressure rise time shorter than 0.5 μs. Manganin gauges in various applications have been investigated for several decades. Bourne (2013) and Ginsberg and Asay (1991) noted that the accuracy of Manganin pressure gauges was higher than that of carbon resistor gauges. Calibration curves for determining the longitudinal and lateral stresses (0~20GPa) measured by commercially available Manganin gauges have been developed through impact experimental studies performed during decades (Rosenberg et al. 1980;

Rosenberg and Moshel 2014). The failure of Manganin gauges at high pressures (60 GPa) is due to the phase transition in the polymer part of the gauge that occurs at the high temperature caused by the shock wave (Rosenberg et al. 2009).

2.2. Shock response of geological material

In production blasts, such as mining application, rock materials adjacent to explosives are commonly subjected to a shock wave with a magnitude not exceeding 20 GPa (Braithwaite 2009; Zhang et al. 2017). Experiments involving impact on plates can easily be designed to give a shock wave up to such magnitude and impact tests are often used when investigating shock response of rock materials (Millett et al. 2000; Willmott and Proud 2007; Kirk 2014; Zhang et al. 2017). When the magnitude of a shock wave is below approximately 20 GPa, the shock response of rock materials is complex since both elastic-plastic behavior and the effects of rock structure, such as flaws and grain size, are involved. For example, Lysne (1970) found that the effects of in-material structure of tuff on the shock Hugoniot should be considered for shock pressure lower than 2.5 GPa. Shock waves in a weak igneous rock (Willmott and Proud 2007) were considered to be hydrodynamic at pressures higher than 4.5 GPa. The investigations about the attenuation of shock wave in rock materials are limited. For example, Nakazawa et al. (2002) investigated shock-wave attenuation in basalt and found that the attenuation depended on the propagation distance raised to the power of -1.7 to -1.8.

2.3. Fractures surrounding the borehole

Previous studies have indicated that a shock wave generates intensely crushed rock in the immediate vicinity of blastholes, resulting in the borehole expansion and the crushed zone. Cunningham et al. (2006) concluded that at least half of the total explosive energy was consumed for the borehole expansion. For the crushed zone, the ratio of the crushed zone diameter to the initial borehole diameter was found to be from 1 to 2.76 in grouted cylinders (Sun 2013), depending on the decoupling ratio and the explosive types, and 2.63 in a concrete block (Iverson et al. 2009). Esen et al. (2003) found this ratio to be at maximum 5 by carrying out blast tests on concrete blocks. They also proposed a model to predict the size of crushed zone.

The shock wave attenuates to a stress wave outside the immediate vicinity of the borehole, and the rock fractures are dominated by the stress wave. Kutter and Fairhurst (1971) found that the radial cracks emerged from the crushed zone and a free surface in the surrounding region favors the generation of radial cracks towards the surface. Banadaki (2010) conducted single-hole blast tests on small-scale granite specimens and found that higher crack densities initiated in granite with smaller grain sizes and higher uniaxial compressive strength. Sun (2013) carried out similar experiments on cement grout specimens and concluded that the extents of crushed zone and fractured zone were controlled by dynamic compressive and tensile strengths, respectively. Dynamic photoelastic analysis is commonly applied to investigate the initiation and propagation of cracks under the stress wave loading. From model blast experiments combined with

dynamic photoelastic analysis, Fourney (2015) emphasized that the combined action of primary wave (P wave) tail and the shear wave (S wave) front interacted with the flaws located either close to or remote from the borehole region, and the reflected stress waves from the free surface reinitiated the arrested cracks between the free surface and the borehole. In addition, the reflected stress waves from the free surface interacted with the outwardly travelling radial cracks (Fourney 2015). When the stress intensity factor at the tip of the radial cracks becomes greater than the fracture toughness of rock after the reflected waves arrive, either circumferentially directed cracks or branching of the radial cracks are initiated, producing a fracture network in the fractured zone (Fourney 2015).

2.4. Rock fragmentation

The fracture network separates rock mass and leads to a large number of fragments, where the fragmentation is taken into consideration. For production blasts in mining, optimum fragmentation is in general defined as that which gives the minimum cost from drilling to grinding, maximum ore recovery, high productivity and minimum effect on safety and environment (Zhang 2016). The free surface is an essential factor to achieve optimum fragmentation. From model blast tests, as well as full-scale blasts, different models has been developed to predict the degree of fragmentation (Djordjevic 1999; Kanchibotla et al. 1999; Hall and Brunton 2002; Ouchterlony 2005). It has been found that fines are predominantly generated in the crushed zone and coarse fragments in the fracture zone. Sanchidrián and Ouchterlony (2017) developed a non-dimensional model for fragmentation in bench blasting, considering the discontinuities spacing and orientation and the delay between successive contiguous shots in the model. Ouchterlony et al. (2017) analyzed sieving data for blasted rock and developed a method, called fragmentation-energy fan, to predict rock fragmentation. The data in the concept was expressed by percentile fragment sizes as function of specific charge, which shows that a set of straight lines tend to converge on a common focal point in a log-log diagram. The approach is also applicable in drop weight testing of rock (Ouchterlony and Sanchidrián 2018).

Swelling space is also essential for rock fragmentation. In multi-hole blasts, swelling space allows fragments to expand so as to complete the process of fragmentation, and further affects the formation of new free surfaces for the immediately subsequent blasthole (Zhang 2016). In sublevel caving, the rock mass is blasted under confined conditions, i.e., limited swelling space for the blasted material. From confining blast tests on concrete blocks, Johansson and Ouchterlony (2011, 2013) found that confined specimens developed coarser fragments than specimens with free surface. For multi-row blasts in open pit mines, Winzer et al. (1983) concluded that more oversize boulders were formed from the first blasthole row than those formed from the other rows. If the swelling space of the rock in front of the first row is large, for instance unlimited, the fragments can move freely, thus the kinetic energy carried by the flying fragments does not contributes to fragmentation.

Free surface movement (burden movement) in blasting has been investigated for several decades and there are many related studies (Bergmann et al. 1973; Chiapetta and Borg 1983; Segarra et al. 2003; Wimmer et al. 2012). In general, it has been found that the burden velocity is related to the explosive energy, the burden distance and the rock type. Sanchidrián et al. (2007) showed that the kinetic energy carried by the moving fragments varied in a range of 3% to 21% of the explosive energy. Zhang (2016, 2017) proposed that the kinetic energy should be utilized to further fragmentation by forcing fragments to collide with the muckpile remaining from the previous blast.

3. Experimental method

3.1. Material testing

The rock applied in this research was medium-grained granite quarried from Fangshan District (Beijing, China). A series of mechanical tests were carried out to determine important parameters. Static properties were obtained using a servo-hydraulic loading machine and dynamic properties were obtained using a Split Hopkins Pressure Bar (SHPB). Uniaxial static compressive strength tests were performed on cylindrical specimens with a 50 mm diameter and a 100 mm length. For static tensile strength, Brazilian tests were performed on disc specimens with a 50 mm diameter and a 20 mm thickness. Dynamic compressive strength tests were performed on cylindrical specimens with a 50 mm diameter and a 50 mm length, and dynamic Brazilian tests on disc specimens with a 50 mm diameter and a 20 mm thickness. For each property, five replicate tests were performed, and the average values listed in Table 1 were determined.

Table 1 Measured properties of Fangshan Granite

Properties	Average
Density (g cm^{-3})	2.74
Young's modulus (GPa)	43.8
Poisson's ratio	0.23
Uniaxial static compressive strength (MPa)	84.1
Static tensile strength (MPa)	6.3
Dynamic compressive strength at 90 s^{-1} (MPa)	130
Dynamic tensile strength at 45 s^{-1} (MPa)	8.0

The major geochemical components of Fangshan Granite are SiO_2 (33.6-56.9 wt%), MgO (5.3-9.4 wt%), and CaO (1.5-14.8 wt%). The dominant heavy mineral is magnetite (1.01 wt%), with grains up to 0.7 mm in size. The grain sizes of other heavy mineral compositions range between 0.02 mm and 1.0 mm.

3.2. Small-scale blasting

The small-scale blast tests performed for this thesis have two different set-ups. Firstly, a cylindrical set-up was used to measure the shock response of granite and to find out the fractures near boreholes. For the tests concerning deformations and fractures on a free surface, a set-up with cubic blocks was applied. All specimens had a centric borehole for the explosive charge and were blasted in an explosion chamber at the Beijing Institute of Technology. The granite cylinder and cube are shown in Fig. 3.1. The test programme

consisted of three parts: measurements of the shock pressure in the blasting, fractures around the blasthole and fracture processes of the blocks. A total of 16 granite cylinders and six granite cubes were blasted as the main tests, on which the conclusions are based. Dimensions and charge weights for these specimens are given in Table 2, and further details are presented in the corresponding papers in PART II. Five cylinders and two cubes were blasted as pretests for this. The results of the pretests are not considered further.

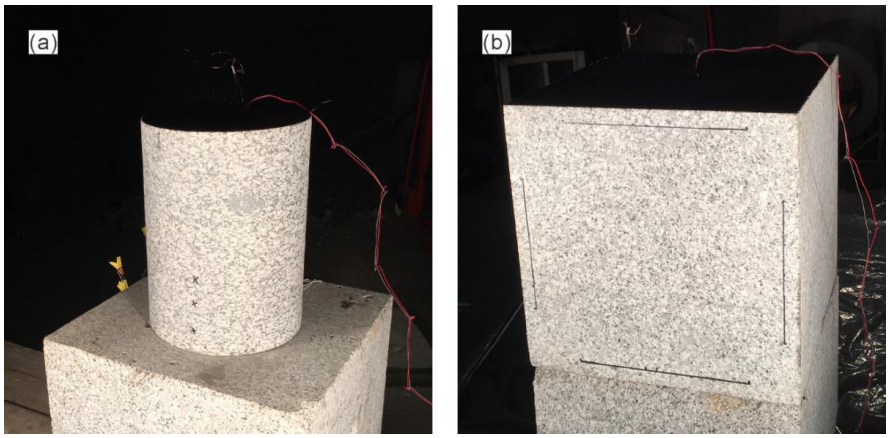

Figure 3.1 Granite specimens used in blast tests; (a) cylinder, (b) cube

3.2.1. Measurements of shock pressure in blasting

The specimens used for the shock pressure investigation were granite cylinders with two different sizes; three cylinders (S1-S3 Paper I, Table 2) had a diameter (D) of 150 mm and a length (L) of 200 mm, while the seven others (S4-S10 Paper I, Table 2) had D 240 mm × L 300 mm. The cylindrical rock specimens were placed on granite support blocks in the blast chamber. To measure the shock pressure and to investigate the shock attenuation, Manganin gauges were embedded in the specimens. Either one or two gauges were used in each specimen. A 24-bit isolation data acquisition device (LTT24, LTT Labortechnik Tasler GmbH) with the integrated signal conditioning module recorded pressure signals. The sampling frequency was set to 4 MHz. The pressure measurement was inspired by plate impact tests reported in the general literature. The configuration of the pressure gauges was based on five pretests and characteristics of the shock wave propagating around a borehole. A concentric hole with a 20 mm diameter for inserting an explosive charge was drilled from one end. A 50 mm diameter and 100 mm length hole was machined from the other end, in order to insert a special designed plug equipped with one or two pressure gauges. Two holes were concentrically connected and the interface was machined to be parallel to the ends. The detailed layout of a D 240 mm granite cylinder is shown in Fig. 3.2, with vertical and horizontal cross-sections. The diameter and the length of the borehole are $D_{borehole}$ and $L_{borehole}$, respectively, and D_{plug} is the diameter of the plug for the pressure measurement. The hole for the insert plug had basically the same dimensions in all specimens. A detonator was placed on the top of the

charge and cement grout was used as stemming. In order to ensure a stable detonation front, a fully coupled charge was applied, made by compressing powder TNT. The pressed TNT had a slightly smaller diameter than the borehole diameter and its density was approximately 1.6 g cm^{-3}.

A steel tube placed outside of each specimen had an external diameter of 300 mm (D_{steel}), a wall thickness of 16 mm (t_{steel}), and a length of 300 mm. The steel tube was provided to investigate the effects of radial constraints on fractures of cylinders. However, the recorded signals showed that the Manganin gauges failed before the stress wave had reflected back from the surface of granite cylinders. Accordingly, the boundary condition on the granite cylinders did not influence the measured shock pressure.

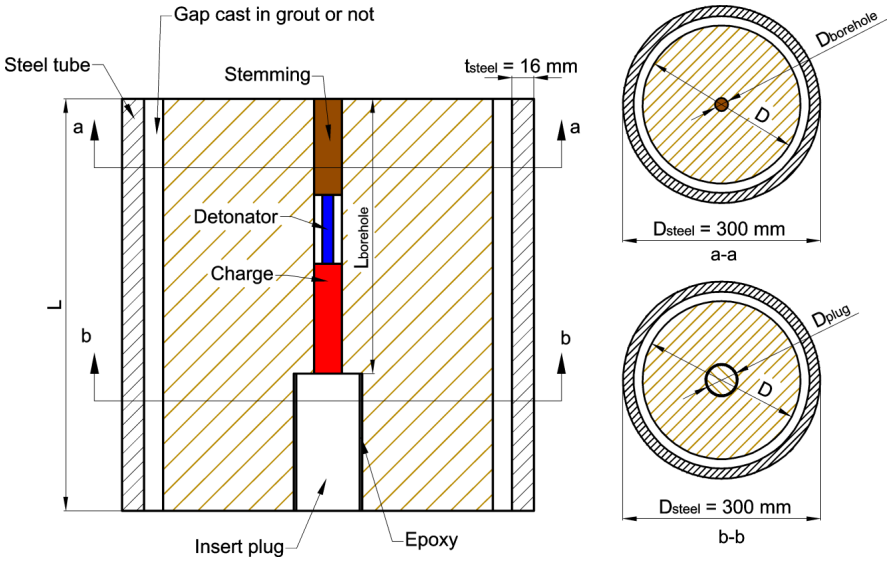

Figure 3.2 Cross-sections of a cylinder specimen with a 240 mm diameter and steel tube

Table 2 Dimensions, charge weights and result items for granite specimens

Paper	Cylindrical specimen	Size of Specimen D (mm) × L (mm)	Charge weight (g)	Shock pressure	Damage zones/ Fractures	Fracturing on surface	Full-field strain	Strain by gauge‡
I	S1	154 × 200	19.83	■				
	S2	149 × 200	20.49	■				
	S3	150 × 200	30.16	■				
	S4	240 × 300	40.10	■				
	S5†	240 × 300	39.38	■	■			T
	S6	240 × 299	39.55	■				
	S7	240 × 300	20.02	■				
	S8††	240 × 300	40.18	■	■			T
	S9	238 × 300	40.11	■				
	S10†††	228 × 300	38.93	■	■			
II	S1	228 × 300	5.61		■			T
	S2	228 × 300	5.47		■			T
	S3	228 × 300	5.52		■			T
	S4	228 × 300	5.46		■			
	S5	228 × 300	5.50		■	■		
	S6	228 × 300	2.00		■			
	S7†	240 × 300	39.38	■	■			T
	S8††	240 × 300	40.18	■	■			T
	S9†††	228 × 300	38.93	■	■			

	Cubic specimen	Size of Specimen (mm^3)	Charge weight (g)			
III	S1	400 × 400 × 400	12.1	■		
	S2	400 × 400 × 400	6.1	■		
	S3	400 × 400 × 400	12.1	■		
	S4	403 × 403 × 401	12.0	■	■	G
	S5	403 × 404 × 403	6.0	■	■	G
	S6	400 × 400 × 400	12.0	■	■	G

‡ Symbol T identifies test with strain gauge attached on steel tube; G identifies test with strain gauges attached on granite surface.

†, ††, †††: Specimens S5, S8 and S10 of Paper I are the same as Specimens S7, S8 and S9 of Paper II, respectively.

The 50 mm diameter insert plug in each specimen was designed to measure the shock wave pressure in the axial direction of granite cylinders. The details about the pressure measurements are described in Paper I. The layouts of the insert plugs are shown in Fig. 3.3. To allow measurements of the shock response at different distances from the explosive, the cylindrical plug was assembled from two or three parts, which are denoted backing cylinder, middle plate and front plate in the figure. To improve the survivability of the Manganin pressure gauges, thin PTFE sheets were used to encapsulate the pressure gauge. A slow cure epoxy was used between the PTFE sheets and the Manganin gauge, and between the granite and the PTFE sheets, to assemble the insert plug. As shown in Fig. 3.4, a clamping fixture with a short hollow steel cylinder was used to align the granite pieces and keep them concentric. The inner wall of the hollow cylinder was lubricated to avoid sticking to the plug. After assembly, the granite surface was cleaned with ethanol. The granite plug was inserted into the 50 mm hole in the granite test cylinder and the 0.25 mm clearance between the plug and the hole was filled up with a slow cure epoxy with a low viscosity.

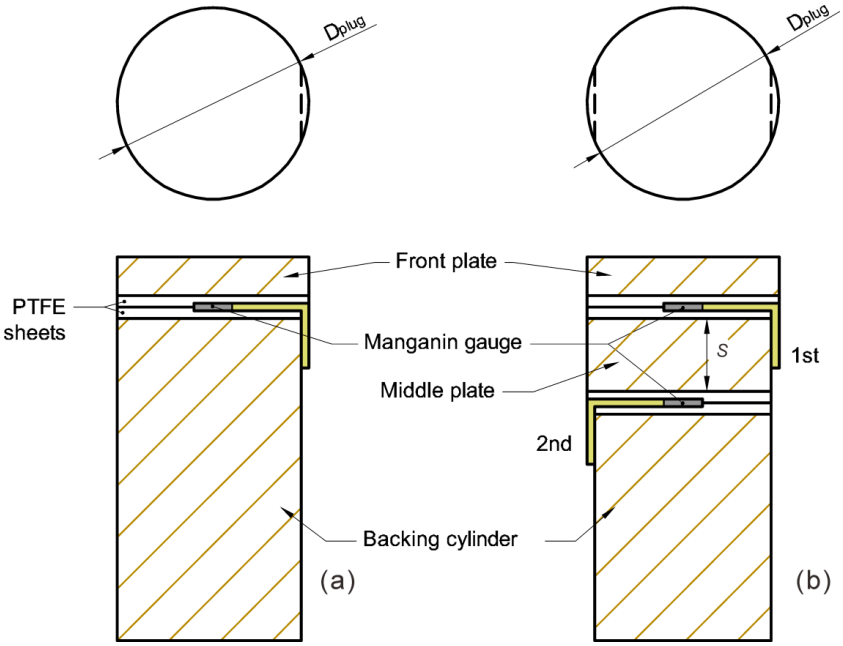

Figure 3.3 Schematic configuration of insert plugs: (a) plug with a Manganin gauge, (b) plug with two Manganin gauges.

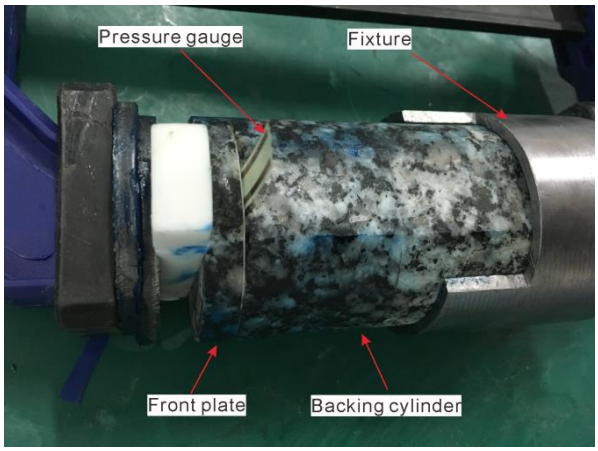

Figure 3.4 Gluing of insert plug with one gauge in fixation clamp

3.2.2. Fractures around the blasthole

In order to investigate the fractures around the blasthole and the effects of the boundary conditions, six granite cylinders (S1-S6 Paper II, Table 2) with dimensions D 228 mm × L 300 mm were placed inside steel tubes. The gap between the granite cylinder and the steel tube was either left empty or filled with gravel or cement grout in the various tests. Each specimen was blasted with a decoupled charge of 2 g or 5.5 g PETN. The density of PETN was approximately 0.9 g cm^{-3} and the charge was positioned in a 14 mm diameter borehole at the center of the cylinder. The detailed charge parameters are given in Paper II. In addition, three large specimens (diameter of 240 mm, S7-S9 Paper II, Table 2) mentioned in the above section were taken into consideration for comparisons.

Three boundary conditions were used in the tests on the cylinders: (1) the gap between granite and steel tube casted with cement grout to simulate a fully confined boundary for the granite cylinders (Fig. 3.5a); (2) the gap filled with an equal ratio mix of 8-mm and 18-mm gravel particles to simulate a partly flexible boundary for the granite cylinders, denoted gravel-confined boundary (Fig. 3.5b); (3) a free lateral surface. According to different swelling spaces, the third boundary condition was subdivided into three cases. The first case is that a 3 mm thick rubber sheet was used as a loose lining between the granite cylinder and the steel tube as a cushion for flying fragments (Fig. 3.5c). For the second, the gap was left empty (Fig. 3.5d). For the last case, the steel tube was omitted and, as a result, the free lateral surface of the granite cylinder had infinite swelling space (Fig. 3.1a). The impedance ratio between the granite and the hardened cement grout was estimated to 1.16 from the material properties, i.e., ensuring a good continuity. The gravel particles that fill in the gaps for some specimens were dip-painted with a blue color to distinguish from broken granite after the tests.

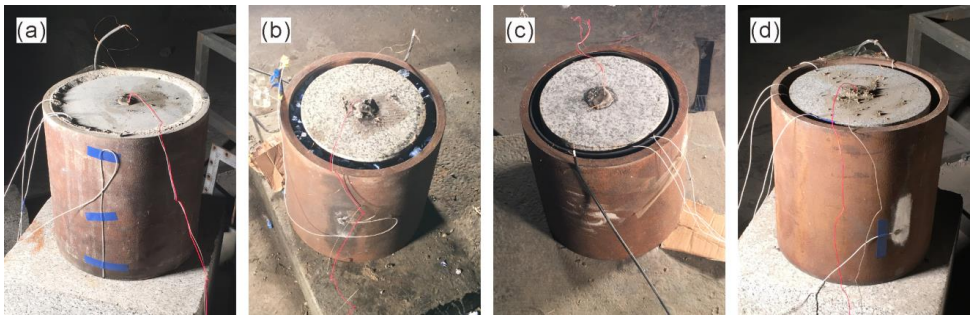

Figure 3.5 Images of typical specimens with different boundaries: (a) fully confined boundary; (b) gravel-confined boundary; (c) rubber cushion; (d) empty gap

To perform an accurate examination of the fractures around the boreholes, the post-blast boreholes in the fully confined specimens were filled with a mixture of epoxy and fluorescent green powder. After the epoxy had cured, the specimens were carefully cut to obtain the cross sections perpendicular to the borehole at 180 mm (cut plane A in Fig. 3.6) and 110 mm (cut plane B in Fig. 3.6) from the specimen bottom. For the specimens with the gravel-confined boundary, the gravel and loose granite fragments at the top end of the specimens were removed to reveal the fractures on the cross-section. Specimens with the free surface fragmented completely and the fragments were collected and analyzed.

To trace the blast actions on the encasing steel tubes, one uniaxial strain gauge was attached along the circumferential direction at each tube to capture hoop strains, as shown in Fig. 3.6. The strain measurement of the steel tube deformation was performed to evaluate the effects of the boundary conditions on the fracture process. The quarter-Wheatstone strain signals were recorded by a LTT24 device. Fracturing of the cylindrical surface of one specimen was monitored by a high speed camera. Details are given in the next section.

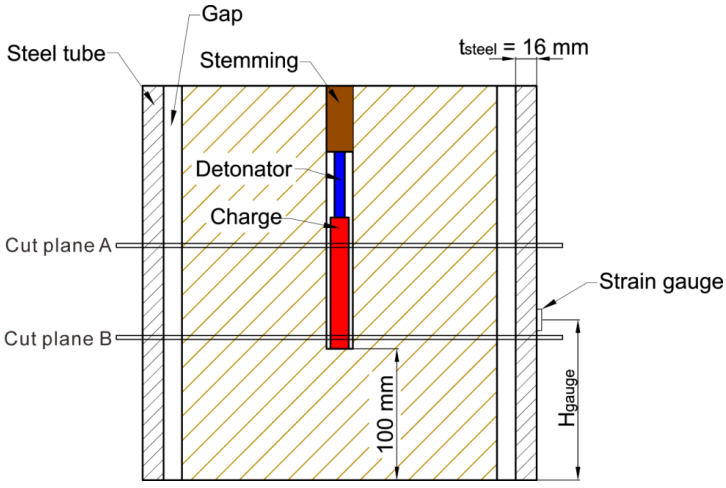

Figure 3.6 Schematic of a cylinder specimen with a 228 mm diameter and a steel tube

3.2.3. Fracture processes of blocks

The set-up was designed to allow monitoring of the fracture process on a free surface during blasting, and is described in detail in Paper III. Granite cubic specimens (S1-S6 Paper III, Table 2) with dimensions of 400 × 400 × 400 mm^3 were used in this set-up and were placed on granite support blocks in the blast chamber to align one lateral surface of the cube with an observation window and a high speed camera. Thus, the specimen to be blasted had contact with the support block on its bottom surface and the five other surfaces were free, as shown in Fig. 3.1b. A fully coupled charge of 6 g or 12 g PETN was applied in a borehole with a 10 mm diameter and a 300 mm length for each specimen.

The high speed camera (Photron Fastcam SA5) was oriented towards a lateral surface, which is defined as the front surface, at a right angle. The distance between the camera lens and the front surface was 3100 mm. Given the distance, the chosen pixel resolution would determine the size of the field of view. Views A and B in Fig. 3.7a correspond to two different camera settings; the former corresponds to a 576 × 600 pixel resolution and a frame rate of 20,000 frames per second (fps), and the latter a 256 × 304 pixel resolution and rate of 75,000 fps. The focus of the settings was on deformations of the free surface and fracture patterns. The digital image correlation (DIC) technique was applied to achieve strain fields on the front surface. This technique has been evaluated by Reu and Miller (2008) and Bornert et al. (2009). Since the granite material had a natural speckle pattern, spray painting on the observed surface was not required. The DIC analysis provides the displacement field on the observed plane through matching pixel subsets in images, which in turn is used to obtain the surface strain field. The focused area for the DIC analysis was a portion of the front surface imaged by the high-speed camera. The reference subset of pixels in the DIC computation was chosen to 27 × 27 pixels and a subset step of 4 pixels.

Three uniaxial strain gauges were mounted on the central line (line parallel to the borehole) to measure transversal strains on the surface opposite the front surface, as shown in Fig. 3.7b. It was assumed that the results of the strain gauge measurements can be compared with the strain data derived from the DIC analysis on the front surface.

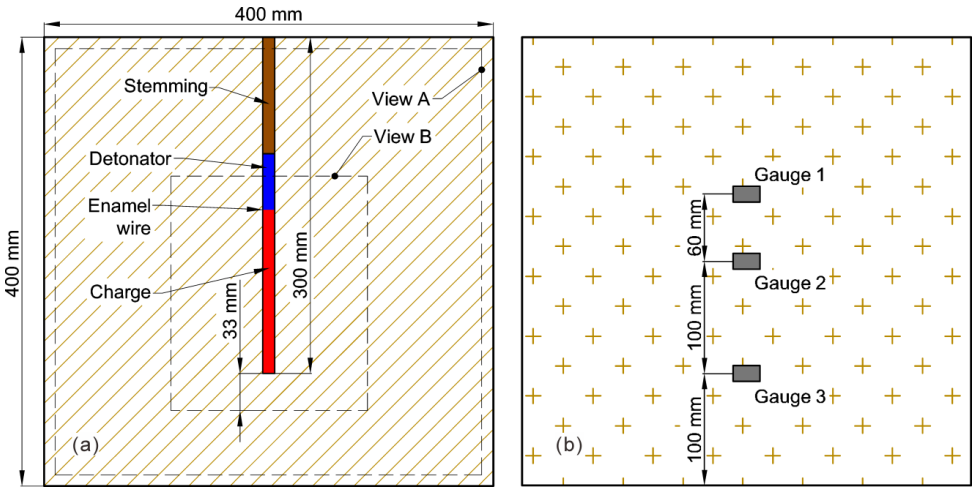

Figure 3.7 Schematic of granite block: (a) vertical cross section; (b) arrangement of strain gauges

One cylindrical specimen with dimensions D 228 mm × L 300 mm was not covered by the steel tube, as shown in Fig. 3.1a. The fracturing of a part of the lateral (cylindrical) surface was monitor by the high speed camera. The distance between the camera lens and the cylinder was 2700 mm. The image resolution of the camera was set to 704 × 520 pixels and the frame rate to 20,000 fps. The field of view is shown in View C in Fig. 3.8.

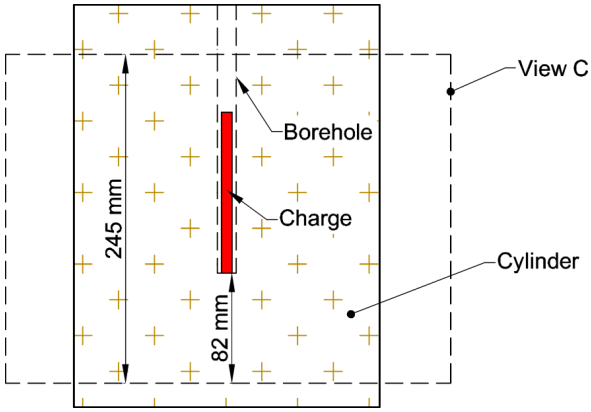

Figure 3.8 Field of view for a cylindrical specimen

4. Results

4.1. Shock pressure histories

A total of ten cylinders were tested in order to measure shock pressures of rock in the vicinity of the blasthole. After performing the blast tests as described in Section 3.2.1, the pressure in each specimen at the monitored positions was determined. Two selected graphs of pressure against time are shown in Fig 4.1, where the response part of the curves is unfiltered. The trigger moment (detonation initiation) is at 256 μs on the time scale. The gauges in most specimens recorded for approximately 3 μs before they failed and successfully captured peak pressures, as shown by the curves in Fig. 4.1a. The recorded peak pressures span from 15.9 GPa at the first gauge to 4.4 GPa at the second gauge and the details are given in Paper I.

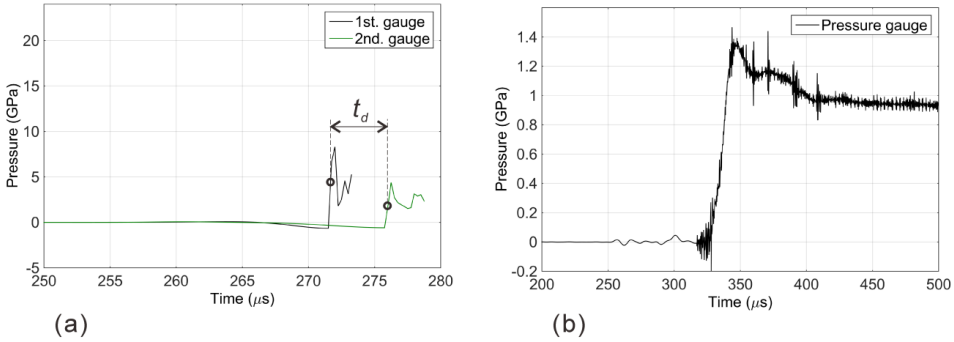

Figure 4.1 Typical pressure traces measured by the Manganin gauges; (a) pressure caused by charge detonation, (b) pressure caused by deflagration of the charge

Fig. 4.1a shows two pressure signals, which are from the first and the second gauges in a specimen, mounted at a distance of 15.8 mm and 36.3 mm from the charge, respectively. For this specimen, the charge weight was 40 g and the peak pressures from the gauges were 8.3 GPa and 4.4 GPa. The pressures increased to the peaks within a time period of 0.5 μs.

Fig. 4.1b shows a completely different pressure curve for another specimen, which was measured 11 mm from the charge (40 g). The peak pressure was 1.35 GPa, which was considerably lower than that of the other specimens, and the rise time was approximately 16 μs much longer. In addition, the pressure gauge survived throughout the recording period, i.e., lasted much longer than the gauges in the other specimens. This was because a deflagration-type explosion occurred in this specimen.

From the pair of pressure gauges in some of the specimens, the shock-wave velocity in the rock can be determined. With the 0.5 μs rise time on the pressure curve, the arrival time of the shock wave at the gauge was taken equal to half of the rise time, and the delay time between two gauges, t_d, is as indicated in Fig. 4.1a. The times for the shock

wave propagating through the PTFE sheets were considered. Accordingly, the velocity of the shock wave propagating through the middle plate, *S* in Fig. 3.3b, was determined. In addition, there were two specimens in which the first gauge failed immediately when the shock wave arrived. The time of the gauge failure was considered as the arrival time of the shock wave. The calculated average velocities through the middle plate ranged from 4.58 mm μs^{-1} to 5.34 mm μs^{-1}, largely depending on the different thicknesses of the front plates, i.e., the effective distances to charges.

4.2. Shock wave attenuation

The measured peak pressures at various gauge locations (7 mm, 15 mm, 23 mm and 35 mm) were used to characterize the shock wave attenuation in the granite. The relation between the peak pressure, *p*, and the travelling distance, *x*, from the explosive has previously been expressed by an empirical experimental relation (Hustrulid 1999):

$$p = A \cdot \exp(-b \cdot x) \qquad (1)$$

Here, *A* and *b* are constants. The constant *A* depends on the initial shock loading on the borehole wall, while *b* is the attenuation factor for the material.

Fig. 4.2 shows a plot of the peak pressure versus the travelling distance as measured in the tests on eight of the present specimens (not considering the specimen with deflagration of the charge, and the specimen with a PTFE plug). The black curve based on a fit applying Eq. (1) is shown in Fig. 4.2, and the fitted constants *A* and *b* are 19.4 GPa and 0.040, respectively, with the corresponding coefficient of determination (R-square) equal to 0.87. The most important observation in Fig. 4.2 is that the data scatter from the fit curve decreases with increasing distance from the explosive.

As the pressure gauges were mounted in the specimens on the length axis and located close to the explosive, the shock wave was considered to be one-dimensional on the location of the gauges. The geometrical spreading in this direction is assume to have a limited effect, and the shock attenuation is mainly dependent on granite damage and fracture and the release wave immediately behind the shock pressure in the detonating explosive. For a given case, the constant *A* may take other values, as it is determined by the initial load conditions, such as type of explosive, borehole and charge diameters, etc. The determined attenuation factor (approximately 0.04 in Fig. 4.2), however, is more likely a combined result of the properties of the tested granite and the explosive (with its rate of release), valid for the investigated pressure range and distance from the charge (respectively 16 GPa to 4 GPa and 0 mm to 40 mm, i.e., two times the diameter of the borehole). In our experiments, by performing curve fitting to the peak pressures for similar gauge configurations (a 0.5 mm-thick PTFE sheet between charge and plug, or not), the constant *A* of the fit curves has a variation of 11-15%. This is explained in depth in Paper I.

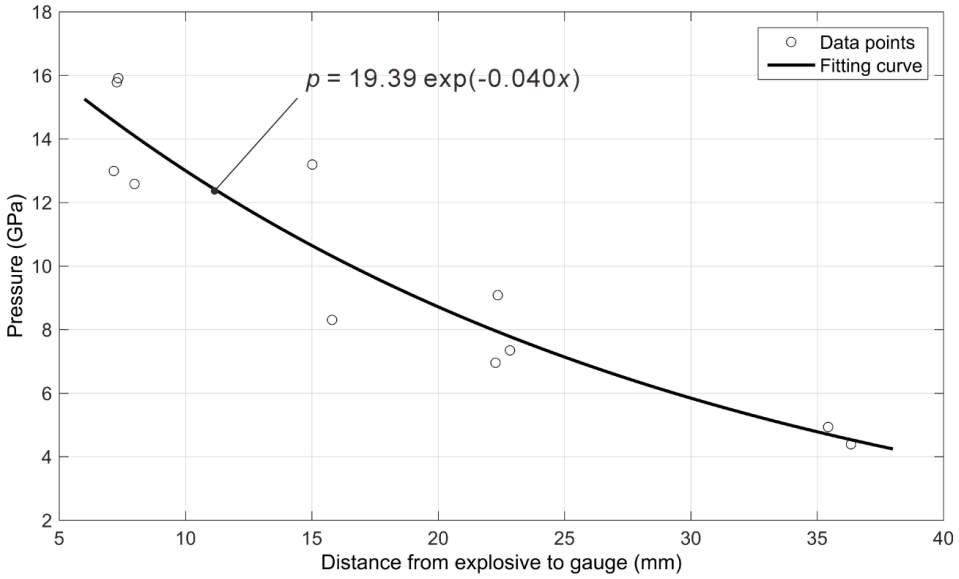

Figure 4.2 Fit curve of the peak pressure in granite

4.3. Damage zones in the vicinity of borehole

A total of nine granite cylinders were considered when investigating the post-blast fractures. The specimens displayed a wide range of damages after blasting. For the fully confined granite cylinders, the damage ranged from a near-intact borehole and a few smaller cracks radiating outwards into the granite to a noticeably enlarged borehole and severe fractures reaching the cylinder boundary. Granite cylinders with the gravel-confinement fragmented into large pieces, i.e., developed radial cracks that split the specimens. For similar charges, the fully confined granite cylinders had significantly less fractures than the gravel-confined specimens. Specimens with a free lateral surface developed severe fractures for the whole body, i.e., fragmentation, and damage around the blasthole could not be determined.

Fig. 4.3 shows the post-blast boreholes of two specimens having charge weights of approximately 5.5 g; Figs. 4.3a and 4.3b are two cross sections of a specimen with fully confined boundary, and Fig. 4.3c is a cross section of a specimen with gravel-confined boundary. After the blasts, the borehole circumferences on the cross-sections appeared quite uneven. The diameter of the expanded borehole, D_{exp}, was taken as the mean diameter of the inscribed and circumscribed circles fitted to the uneven circumference of the post-blast borehole. The initial borehole diameter was 14 mm, and the determined diameters of the post-blast borehole from cut planes A and B (Fig. 3.6) were 14.9 mm and 15.6 mm, respectively. The larger value at the lower cut plane may be due to the higher pressure from the interaction between the shock wave and the borehole bottom, i.e., normal incidence, than the pressure at the upper plane. Fig. 4.3c shows the post-blast boreholes at the cross section approximately 160 mm from the top end of the cylinders.

As shown, severe fractures are formed in the specimens. The blue-colored fragments in Fig. 4.3c are crushed pieces of the gravel fill. For this particular specimen, the determined post-blast borehole diameter was approximately 21 mm. To characterize the borehole expansion, an expansion ratio, denoted m_{exp}, has been defined (Zhang 2016):

$$m_{exp} = \frac{D_{exp}}{D_{borehole}} \qquad (2)$$

Fig. 4.4 shows the experimentally determined borehole expansion ratios versus the corresponding decoupling ratios, and includes experimental data from other studies on rock and concrete materials (Persson et al. 1969; Brinkmann 1990; Cunningham et al. 2006). For specimens with two cut planes, the expansion ratios at the lower cross section are plotted in the figure. The dashed lines in Fig. 4.4 are the boundaries for the observed expansion ratios. The values obviously depend on the decoupling ratio, the properties of the explosive, such as the density and the VOD, and the strength of the blasted material and the given confinement. The details are given in Paper II.

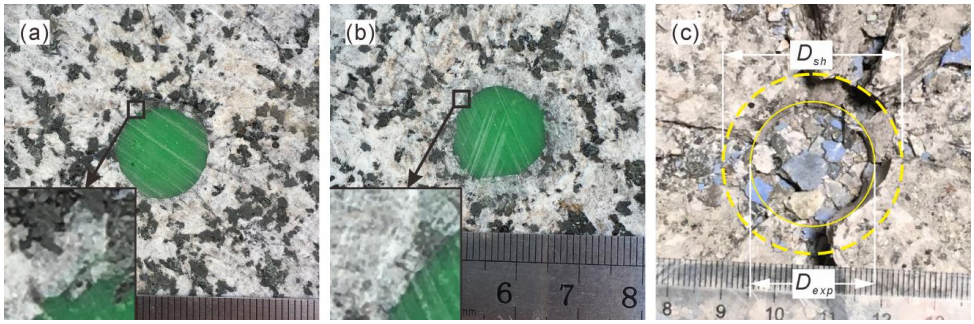

Figure 4.3 Cross sections surrounding post-blast boreholes: (a) a specimen with fully confined boundary (cut plane A), (b) the same specimen (cut plane B) and (c) a specimen with gravel-confined boundary

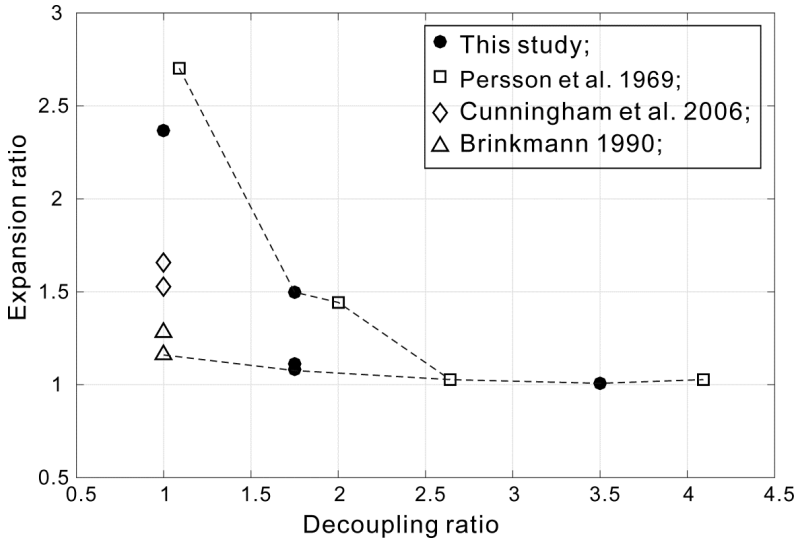

Figure 4.4 Expansion ratio vs. decoupling ratio, present tests and other studies

Figs. 4.3a and 4.3b show that the granite texture near the post-blast borehole is clearly different from the outer zones, i.e., the granite color is quite different. The insert figures show dense radial cracks and some circumferential cracks. The outermost range of the crack network is defined as the boundary of the crushed zone. The diameter of the crushed zone (D_{sh}) for cut planes A and B were 20.5 mm and 21.9 mm, respectively. For the specimen with the gravel-confined boundary, the granite in the near field of the post-blast borehole formed severe fractures. Some crushed granite was removed. The circumferential cracks around the borehole defined the outer boundary of the crushed zone, as shown in Fig. 4.3c. The diameter of the crush zone in the specimen was 27.7 mm. Further discussions are provided in Paper II, which presents that as the decoupling ratio is close to or greater than 3.5, the ratios of the crushed zone are close to 1, meaning no crushed zone.

Under similar charge conditions, a specimen with gravel-confined boundary generated a larger borehole expansion and crushed zone extent than specimens with fully confined boundary. The granite cylinder with gravel-confinement had a partly flexible boundary, which allowed radial movement of the fragments. The annular ring widths, i.e., ($D_{sh} - D_{exp}$) / 2, of the crushed zone, were 3.2 mm and 3.4 mm for fully confined and gravel-confined boundaries, respectively. The values are quite similar, which indicates that the large borehole expansion for the gravel-confined boundary was affected by the radial displacement of the fragments.

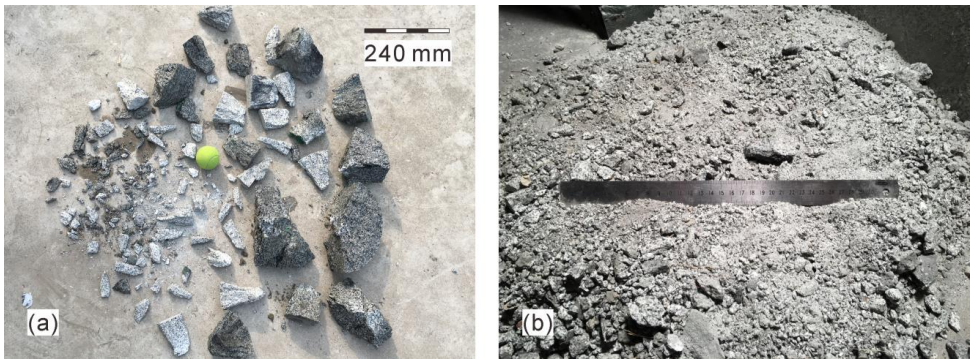

Figure 4.5 Fragments of specimens: (a) 40 g and full confinement and (b) 40 g and empty gap

Fig. 4.5 shows the collected fragments of two specimens, which had approximately 40 g charges (Paper II). The major fragments of the specimen with fully confined boundary in the test are shown in Fig. 4.5a (approximately 10% of the body of this specimen (S7) is missing as the top part of the cylinder was blasted away). As shown in Fig. 4.5b, the fragments of another specimen (S8), which had an empty gap (i.e. free surface) in the test, are much finer. Almost all of the fragments for the latter are less than 1 cm in size. The free surface reflected a tensile wave which contributed to the fracturing of the granite, and the subsequent collisions between the flying fragments and the steel tube may have led to a secondary fragmentation.

4.4. Fracturing on the surface

A total of seven specimens were considered to investigate the fracturing on the surface; six cubic blocks and one cylinder. For specimens with free lateral surfaces, fracture processes were monitored by the high speed camera during the blasting. The high-speed camera was triggered at the initiation of the detonator, which defines the time zero in the frames. Fig. 4.6 shows fracture patterns for three typical specimens; a cylindrical specimen was monitored in View C (Fig. 3.8) and two cubic specimens were monitored in View A (Fig. 3.7a). Although the specimens had different shapes and different charge weights, the fracture patterns consist of clearly visible vertical cracks and less visible horizontal cracks. This illustrates that the expansion occurred mainly in the lateral direction, i.e., transverse to the charge axis. The cylindrical specimen developed severe fractures at time 500 μs as it had a higher specific charge. For cubic specimens, at 1500 μs, the specimen with a greater charge initiated more dominant cracks in the vertical direction than the specimen with lower charge. The visible crack in frames is defined as a macroscopic crack here. By studying the frames, for the cubic specimens with a 12 g charge, the macroscopic cracks initiated in the range of 167 μs to 180 μs after the trigger moment. For the cubic specimens with a 6 g charge, the initiation time of the macroscopic cracks was 225 μs. The details are given in Paper III. In addition, gas products ejected from some cracks at the monitored surface, as noted by arrows in Fig. 4.6. By studying the frames, for the three specimens in Fig. 4.6, the first gas ejection

was detected in the 450 µs, 900 µs and 1,400 µs frames, respectively. The frames in the figure clearly show that gas products did not escape from all of cracks, especially not from the earliest formed cracks. This may imply that dominant cracks at monitored surface did not initiate from the borehole.

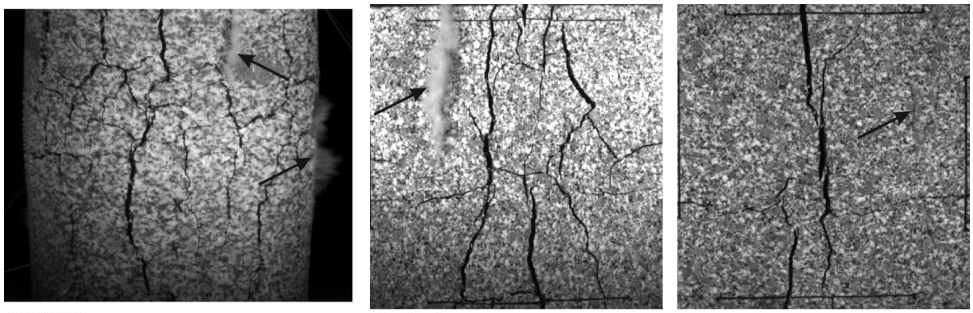

Figure 4.6 Fracture patterns of specimens

By studying the frame series for the cylindrical specimen, the movement of the surface was traced and the determined velocity was at maximum 25.3 m/s. The movement of the cylindrical surface can be compared to a burden movement in an actual bench blasting. In Fig. 4.7, the burden velocity is plotted against the ratio of the burden to the borehole radius. The figure also includes results from other studies (Bergmann et al. 1973; Segarra et al. 2003; Wimmer et al. 2012; Petropoulos et al. 2018) and shows that burden velocity decreases from 43.5 m/s to 1.8 m/s with increasing burden-to-borehole-radius. An exponential relation appears to fit relatively well. By performing a curve fit, the relation can be expressed by:

$$V_B = 64.6 \cdot \exp\left(-0.03 R_h\right) \qquad (3)$$

Here, V_B is the burden velocity and R_h is the ratio of burden to borehole-radius. The burden velocity determined for the cylinder (S5 in Paper II) agrees well with Eq. (3). Note that fully coupled charges were used in the other studies, while our specimen (S5) had a decoupled charge. To allow the comparison, the charge radius for the cylinder was used to replace the borehole radius. In addition, the in-plane velocities of corner fragments of cubic specimens were estimated in the range of 3.1 m s^{-1} to 7.4 m s^{-1}, and the details are given in Paper III.

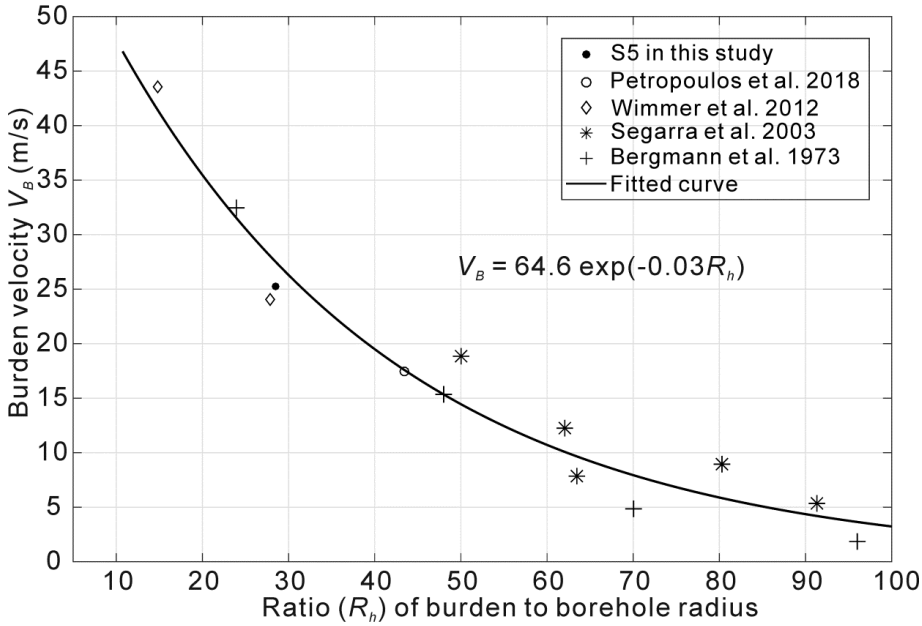

Figure 4.7 Burden velocities vs. ratio of burden to borehole radius; cylindrical specimen and other studies

4.5. Strain measurements

4.5.1. Strains on granite surface

Full-field strains at the monitored surface were evaluated for the cubic specimens with charge weights of 12 g and 6 g. An image resolution of 576 × 600 pixels and frame rate of 20,000 fps was used, corresponding to a time resolution of 50 µs. This camera configuration captured an area of approximately 380 × 395 mm^2, as indicated by View A in Fig. 3.7a, and the chosen field for the DIC analysis was approximately 330 × 330 mm^2, covering the zone of interest on the front surface. Fig. 4.8 shows the color plots of the obtained surface strain fields at time 200 µs after the detonation initiation. The strain fields presented here represent the first principal strain based on the strain components in the XY-coordinate plane (specimen surface).

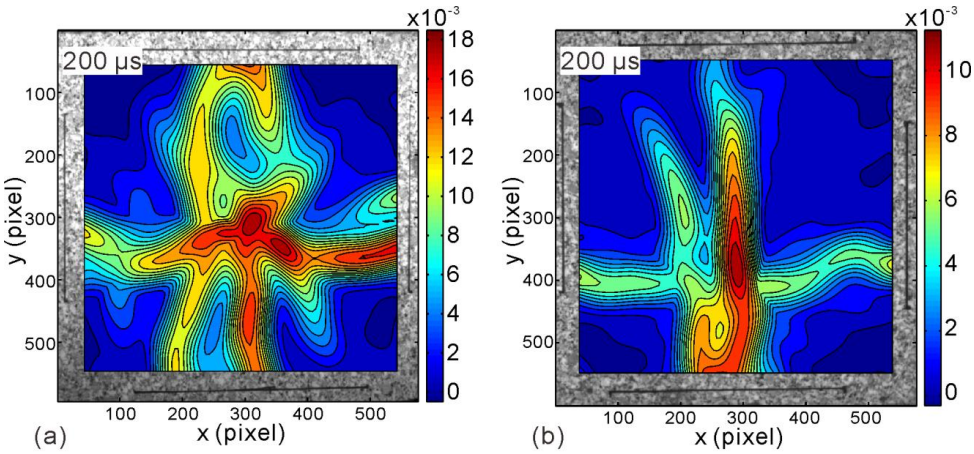

Figure 4.8 Plots of the strain field obtained from the frames recorded through View A: (a) cubic specimen with 12 g PETN; (b) cubic specimen with 6 g PETN

The strain fields in Fig 4.8 mainly consist of some dominant strain concentration zone in the vertical direction and a secondary strain concentration in the horizontal direction. Comparing Figs. 4.8a and 4.8b, we observe the following: (1) a larger charge weight results in a wider vertical strain concentration zone, i.e., two vertical concentration zones, and a higher strain amplitude in the concentration zones; (2) there is only one horizontal strain concentration zone in both specimens; (3) the vertical position of the horizontal strain zone is located higher in the specimen with the longer charge.

The strains were mainly biaxial tensile and the main potential failure areas on the front surface could be easily estimated. It was found that the increased charge length mainly influenced the range of the vertical strain concentration zone.

To further investigate the strain field on the surface, a specimen with the charge weight of 12 g was monitored using a high frame rate and a low pixel resolution (75,000 fps and 256 × 304 pixel resolution). An area of 175 × 208 mm^2 was imaged (View B in Fig. 3.7a). The chosen field for the DIC analysis was approximately 154 × 187 mm^2,

corresponding to the colored areas in Fig. 4.9. The dashed square in the 80 μs frame in Fig. 4.9 shows the location of the explosive charge, and the white rectangle indicates the detonator.

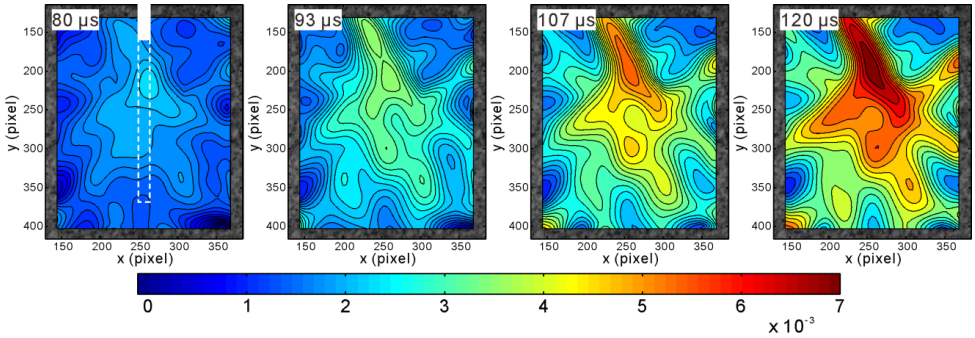

Figure 4.9 Plots of the strain field obtained from the frames recorded through View B

Fig. 4.9 shows four color plots of the strain field (first principal strain, range of strain is 0 to 0.007) for the blasting of one specimen. These plots provide a good picture of the developing strains. From the figure, it can be seen that at 80 μs, the strain is concentrated at the position corresponding to the top of the charge, with magnitude of approximately 2,000 microstrain (με). In the following frames, the strain concentration zone extends to a large area, and strain values increases. At 120 μs, the strain at the position corresponding to the top of the charge reaches the maximum, 7,000 με. After a crack is formed on the surface, the strains derived from the DIC analysis are obviously no longer accurate, as crack opening will be included in the derived surface displacements.

With the centric charge, we may assume that all four sides of the specimen develop quite similar strains. Accordingly, the strains measured on the back surface were compared with the strains measured on the front surface. The horizontal strains on the back surface were measured by strain gauges, as shown in Fig. 3.7b. A combination of strain gauge and DIC data was employed to estimate the crack initiation time. Fig. 4.10 shows the strain curves measured by the three strain gauges on a given specimen. The horizontal strains determined from the DIC analysis for the same specimen at the position corresponding to gauge 2 (red circles) are also plotted in the figure, corresponding to the first six frames after detonator initiation. The strain error in the DIC prediction caused by the out-of-plane displacement of the specimen is accounted for in Fig 4.10 (discussed in Paper III).

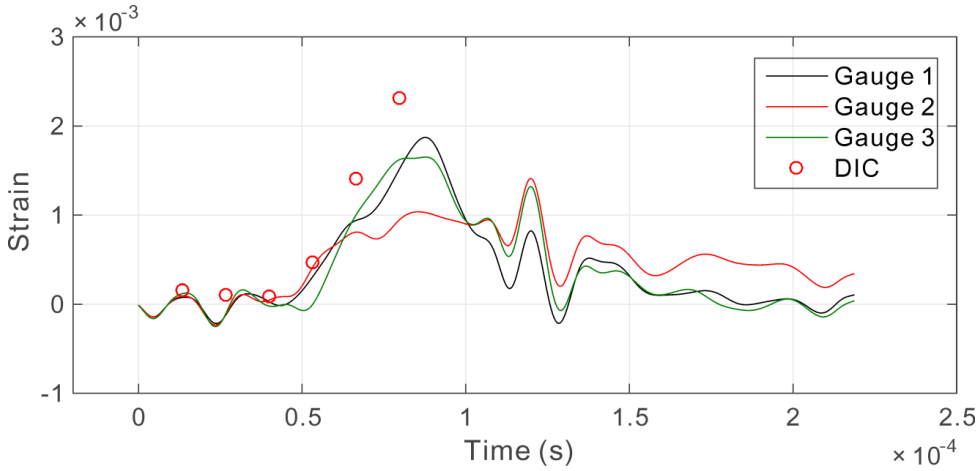

Figure 4.10 Strain measurements on the back surface

As seen in Fig. 4.10, the strain derived from the DIC analysis is 460 με at time 53.3 μs (the fourth circle from the left). The strain measured by gauge 2 (red curve) is 420 με, i.e., quite similar. At 67 μs, the DIC strain is 1,400 με, which is considerably higher than the strain 810 με from gauge 2. This could be because a crack initiated around gauge 2 and released the stress in the region. Accordingly, we may assume that the first crack on the surface initiated 67 μs after the trigger moment.

4.5.2. Strains on steel tubes

To investigate the blast actions on the steel tubes confining the cylindrical specimens, strain gauges were glued on the steel tubes in the circumferential direction (hoop strains). The different materials that filled in the gaps between granite and steel significantly influenced the strains in the steel tubes. Remember that three types of boundary conditions were applied for the granite cylinders; full confinement, gravel-confinement and empty gap. Fig. 4.11 shows the strain curves for five specimens; three with small charges (approximately 5.5 g PETN) and two with large charges (approximately 40 g TNT). The numbering of the specimens is as in Paper II.

For Specimens S1 and S2, which had fully confined boundary and similar charge weights, the measured steel strain histories are quite similar. S7 with large charge weight and fully confined boundary shows much higher strains in the steel than S1 and S2 (small charges) in the whole duration. The peak steel strain for S7 is more than two times the peak strains for S1 and S2. Yield strain of the steel is approximately 1,500 με. The steel tubes had visible but small deformations after the tests, with a barrel-shape (~1 mm increased diameter). Specimens S1, S2 and S3 had similar charge weights. S3, with the gravel-confined boundary, developed lower steel strains than S1 and S2. The low strain therefore indicates that the blast load transmitted to the confining tube was significantly reduced by the gravel layer.

S8 produced a lower strain compared to S7, and a later response time, which may result from the time that the fragments need to travel across the gap and impact the steel wall. Also for this specimen the steel strain is above the yield strain, which corresponds to a small permanent deformation of the steel tube.

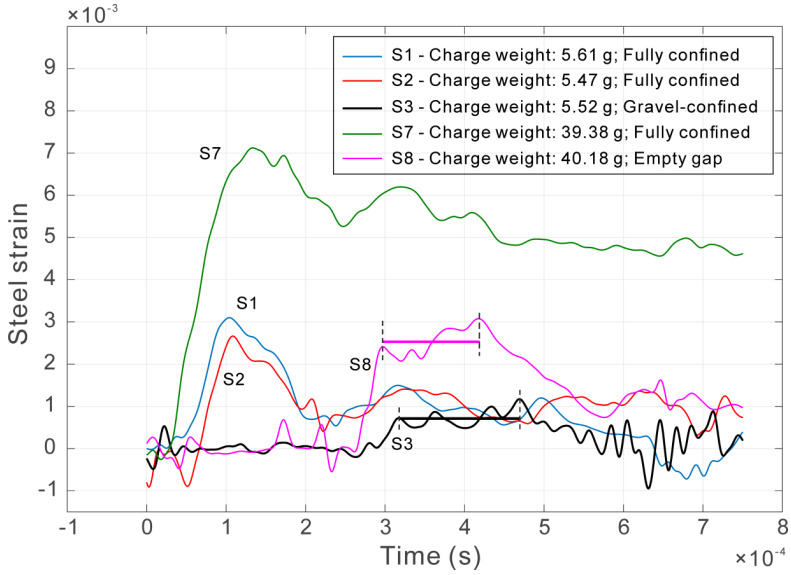

Figure 4.11 Hoop strain in steel tubes

5. Summary

5.1. Conclusions

Four objectives were outlined in the start of this thesis, and are answered as follows:

Conclusion 1

Pressures of shock waves were measured at distances of 7, 15, 22 or 35 mm from the explosive charge, and peak pressure values ranged from 15.9–4.4 GPa, mainly depending on the distances, with rise times of ~0.5 μs. For the specimen that experienced charge deflagration, the peak pressure was 1.35 GPa at a distance of 11.0 mm from the explosive, with a 16 μs rise time. The measured velocities of the shock wave propagating through the granite ranged noticeably from 5.34 mm μs^{-1} to 4.58 mm μs^{-1}, mainly depending on the distance from the explosive. By assuming an exponential relation between the peak pressure and the distance from the explosive, the attenuation factor obtained from curve fitting was 0.04.

Conclusion 2

For the specimen with fully confined boundary, the borehole expanded to 2.37 times the initial borehole diameter at the decoupling ratio of 1, i.e., the fully coupled charge. As the decoupling ratio was 3.5, the ratios of the crushed zone and the expansion ratios were close to 1, i.e., no crushed zone and no borehole expansion. The present results in combination with experimental data from the previous studies indicated that the borehole expansion and the size of the crushed zone depended heavily on the decoupling ratio, the properties of the explosive, such as the density and the VOD, and the given confinement. The cylinders confined by gravel fill developed more and longer radial cracks than the cylinders confined by cement fill. In addition, the strain measured on the steel tube of these specimens indicates that the blast load transmitted to the confining tube was significantly reduced by the gravel layer. For a cylinder with an empty gap between its surface and a confining steel tube, fragment collisions with the steel tube caused significant hoop strains in the steel, indicating a secondary fragmentation.

Conclusion 3

For the cubic specimens, the increase in charge length mainly influenced the number of dominant vertical cracks rather than the number of dominant horizontal cracks. The initiation time for the macroscopic cracks was markedly affected by the charge weight of specimens. The ejection of gaseous products from the cracks on the specimen surface did not occur simultaneously with the macroscopic cracks. From the in-plane motion of corner fragments, it was found that the translational velocities were directed mainly transversely to the charge axis and that the velocity magnitudes (3.1 m s^{-1} to 7.4 m s^{-1}) were influenced by the charge weights. For a cylinder with a free cylindrical surface, the moving velocity of the surface (burden velocity) was 25.3 m s^{-1}. Combining with other

studies, we found that the burden velocity had an exponentially decreasing trend for an increasing ratio of the burden to the borehole radius.

Conclusion 4

The dominant cracks observed on the front surface were initiated from or around the surface rather than from cracks radiating from the borehole. For the cubic specimen with a 12 g charge, the first crack initiation was found to occur at 67 μs after detonation. The maximum concentration of strains from the DIC analysis corresponded well with the actual fracture pattern on the monitored front surfaces, showing that the DIC technique may be successfully applied in the detection and development of multiple cracks caused by blasting.

5.2. Suggestions for future research

Small-scale tests were performed on granite cubes and cylinders with a single blasthole in this study. The following suggestions for further research are given:

Measurements of shock pressure in the radial direction of a blasthole

To further investigate shock compression around the blasthole, it is suggested to develop a proper detection method for measuring shock pressures in the radial direction, i.e., a diverging shock wave loading on the rock in the near field of blastholes.

Strain development on specimen surfaces

To entirely avoid the uncertainties in the strain field measurements, caused by out-of-plane motion in the current study, it is suggested that full 3D DIC analysis is performed in similar studies on cylindrical or planar surfaces of specimens. This will also provide more accurate information on 3D motion of fragments.

Fragmentation

Due to limited resources in this study, the size distribution of fragments was not carried out systematically and thoroughly enough. More information on the size distribution in various blast experiments should in general be acquired.

References

Banadaki MMD (2010) Stress-wave induced fracture in rock due to explosive action. University of Toronto

Bergmann OR, Riggle JW, Wu FC (1973) Model rock blasting-effect of explosives properties and other variables on blasting results. Int J Rock Mech Min Sci 10:585–612. doi: 10.1016/0148-9062(73)90007-7

Bornert M, Brémand F, Doumalin P, et al (2009) Assessment of digital image correlation measurement errors: methodology and results. Exp Mech 49:353–370

Bourne N (2013) Materials in mechanical extremes: fundamentals and applications. Cambridge University Press

Braithwaite C (2009) High strain rate properties of geological materials. University of Cambridge

Brinkmann JR (1990) An experimental study of the effects of shock and gas penetration in blasting. In: Proceedings of the 3rd International Symposium on Rock Fragmentation by Blasting. pp 55–66

Chiapetta RF, Borg DG (1983) Increasing productivity through field control and high-speed photography. In: Proc., 1st Int. Symp. on Rock Fragmentation by Blasting. Lulea, Sweden. pp 301–331

Cunningham C, Sellers EJ, Szendrei T (2006) Cavity expansion energy applied to rock blasting. In: European Federation of Explosive Engineers Conference

Davies F, Smith E, De La Cruz C (1997) The measurement of detonation waves in composite explosives. In: Proceeding of the 13th Anaual Symposium on Explosives and Blasting Research. International Society of Explosives Engineers, Las Vegas, Nevada, pp 145–159

Djordjevic N (1999) A two-component model of blast fragmentation. In: AusIMM Proceedings. pp 9–13

Esen S, Onederra I, Bilgin HA (2003) Modelling the size of the crushed zone around a blasthole. Int J Rock Mech Min Sci 40:485–495

Field JE, Ladegaard-Pedersen A (1971) The importance of the reflected stress wave in rock blasting. Int J Rock Mech Min Sci Geomech Abstr 8:213–226

Fourney WL (2015) The role of stress waves and fracture mechanics in fragmentation. Blasting Fragm 9:83–106

Fourney WL, Barker DB, Holloway DC (1981) Model studies of explosive well stimulation techniques. Int J Rock Mech Min Sci Geomech Abstr 18:113–127. doi: 10.1016/0148-9062(81)90737-3

Fourney WL, Barker DB, Holloway DC (1983) Model studies of well stimulation using propellant charges. Int J Rock Mech Min Sci Geomech Abstr 20:91–101. doi:

10.1016/0148-9062(83)90330-3

Ginsberg MJ, Asay BW (1991) Commercial carbon composition resistors as dynamic stress gauges in difficult environments. Rev Sci Instrum 62:2218–2227. doi: 10.1063/1.1142340

Hall J, Brunton I (2002) Critical comparison of Julius Kruttschnitt Mineral Research Centre (JKMRC) blast fragmentation models. Fragblast 6:207–220

Hustrulid WA (1999) Blasting principles for open pit mining: general design concepts. Balkema

Iverson SR, Hustrulid WA, Johnson JC, et al (2009) The extent of blast damage from a fully coupled explosive charge. In: Sanchidrián JA (ed) Proceedings of the 9th International Symposium on Rock Fragmentation by Blasting, Fragblast. CRC Press/Balkema, Granada, Spain, pp 459–468

Johansson CH, Persson P-A (1970) Detonics of high explosives. Academic Press

Johansson D, Ouchterlony F (2011) Fragmentation in small-scale confined blasting. Int J Min Miner Eng 3:72–94

Johansson D, Ouchterlony F (2013) Shock wave interactions in rock blasting: the use of short delays to improve fragmentation in model-scale. Rock Mech rock Eng 46:1–18

Kanchibotla SS, Valery W, Morrell S (1999) Modelling fines in blast fragmentation and its impact on crushing and grinding. In: Explo '99–A conference on rock breaking, The Australasian Institute of Mining and Metallurgy, Kalgoorlie, Australia. pp 137–144

Kirk S (2014) Shock compression and dynamic fragmentation of geological materials. University of Cambridge

Kutter HK, Fairhurst C (1971) On the fracture process in blasting. Int J Rock Mech Min Sci Geomech Abstr 8:181–202. doi: 10.1016/0148-9062(71)90018-0

Lu W, Leng Z, Chen M, et al (2016) A modified model to calculate the size of the crushed zone around a blast-hole. J South African Inst Min Metall 116:412–422

Lysne PC (1970) A comparison of calculated and measured low-stress Hugoniots and release adiabats of dry and water-saturated tuff. J Geophys Res 75:4375–4386. doi: 10.1029/JB075i023p04375

Mencacci S, Chavez R (2005) The measurement and analysis of detonation pressure during blasting. In: Brighton Conference Proceedings, European Federation of Explosives Engineers. pp 231–236

Meyers MA (1994) Dynamic behavior of materials. John wiley & sons

Millett JCF, Tsembelis K, Bourne NK (2000) Longitudinal and lateral stress measurements in shock-loaded gabbro and granite. J Appl Phys 87:3678–3682. doi: 10.1063/1.372399

Nakazawa S, Watanabe S, Iijima Y, Kato M (2002) Experimental investigation of shock wave attenuation in basalt. Icarus 156:539–550. doi: 10.1006/icar.2001.6729

Nie S (1999) Measurement of borehole pressure history in blast holes in rock blocks. In: Proceedings 6th International Symposium on Rock Fragmentation by Blasting. South African Institute of Mining and Metallurgy, Johannesburg, South Africa, pp 91–97

Ouchterlony F (2005) The Swebrec© function: linking fragmentation by blasting and crushing. Min Technol 114:29–44

Ouchterlony F, Sanchidrián JA (2018) The Fragmentation-Energy Fan Concept and the Swebrec Function in Modeling Drop Weight Testing. Rock Mech Rock Eng 1–28

Ouchterlony F, Sanchidrián JA, Moser P (2017) Percentile fragment size predictions for blasted rock and the fragmentation–energy fan. Rock Mech Rock Eng 50:751–779

Persson PA, Ladegaard-Pedersen A, Kihlström B (1969) The influence of borehole diameter on the rock blasting capacity of an extended explosive charge. Int J Rock Mech Min Sci Geomech Abstr 6:277–284

Petropoulos N, Wimmer M, Johansson D, Nordlund E (2018) Compaction of Confining Materials in Pillar Blast Tests. Rock Mech Rock Eng 51:1907–1919. doi: 10.1007/s00603-018-1447-8

Reu PL, Miller TJ (2008) The application of high-speed digital image correlation. J Strain Anal Eng Des 43:673–688. doi: 10.1243/03093247JSA414

Rosenberg Z, Ginzberg A, Dekel E (2009) High shock pressure measurements using commercial manganin gauges. Int J Impact Eng 36:1365–1370. doi: 10.1016/j.ijimpeng.2009.03.012

Rosenberg Z, Ginzburg A, Ashuach Y (2007) More on commercial carbon resistors as low pressure gauges. Int J Impact Eng 34:732–742. doi: 10.1016/j.ijimpeng.2006.02.006

Rosenberg Z, Moshel G (2014) Revisiting the calibration of manganin gauges for lateral stress measurements in shock-loaded solids. J Appl Phys 115:. doi: 10.1063/1.4868296

Rosenberg Z, Yaziv D, Partom Y (1980) Calibration of foil-like manganin gauges in planar shock wave experiments. J Appl Phys 51:3702–3705. doi: 10.1063/1.328155

Rossmanith HP, Uenishi K (2006) The mechanics of spall fracture in rock and concrete. Fragblast 10:111–162

Saharan MR, Mitri HS, Jethwa JL (2006) Rock fracturing by explosive energy: review of state-of-the-art. Fragblast 10:61–81

Sanchidrián JA, Ouchterlony F (2017) A distribution-free description of fragmentation by blasting based on dimensional analysis. Rock Mech Rock Eng 50:781–806

Sanchidrián JA, Segarra P, López LM (2007) Energy components in rock blasting. Int J Rock Mech Min Sci 44:130–147. doi: 10.1016/j.ijrmms.2006.05.002

Segarra P, Sanchidrián JA, López LM (2003) Analysis of bench face movement in quarry blasting. In: Holmberg R (ed) the 2nd World Conference on Explosives and Blasting Technique. Balkema, Rotterdam, pp 485–495

Sun C (2013) Damage zone prediction for rock blasting. Department of Mining Engineering, University of Utah

Taylor NE, Braithwaite CH, Morley MJ, et al (2009) Explosive-rock interactions; experimental study. In: AIP Conference Proceedings. pp 1139–1142

Wang L (2011) Foundations of stress waves. Elsevier

Willmott GR, Proud WG (2007) The shock Hugoniot of Tuffisitic Kimberlite Breccia. Int J Rock Mech Min Sci 44:228–237. doi: 10.1016/j.ijrmms.2006.07.006

Wimmer M, Nordqvist A, Ouchterlony F, et al (2012) Burden movement in confined drift wall blasting tests studied at the LKAB Kiruna SLC mine. In: International Symposium on Rock Fragmentation by Blasting: 24/11/2012-29/11/2012. CRC Press/Balkema, pp 373–383

Winzer SR, Anderson DA, Ritter AP (1983) Rock fragmentation by explosives. In: Proceedings of the 1st International Symposium on Rock Fragmentation by Blasting. p 225

Zhang QB, Braithwaite CH, Zhao J (2017) Hugoniot equation of state of rock materials under shock compression. Philos Trans R Soc A Math Phys Eng Sci 375:20160169. doi: 10.1098/rsta.2016.0169

Zhang ZX (2016) Rock fracture and blasting: theory and applications. Butterworth-Heinemann

Zhang ZX (2017) Kinetic energy and its applications in mining engineering. Int J Min Sci Technol 27:237–244

PART II

Appended journal papers

Paper I

Measurement of shock pressure and shock-wave attenuation near a blast hole in rock

Paper II

Experimental investigation of blast-induced fractures in rock cylinders

Paper III

Fracture processes in granite blocks under blast loading;

The papers are not included in NTNU Open due to copyright

PART III

Appended conference papers

Conference paper I

Chi LY, Zhang ZX, Aalberg A, Yang J (2018) An experimental investigation of fracture patterns near a blasthole in cylinders of granite under different radial confinements. In: Schunnesson H, Johansson D (eds) 12th International Symposium on Rock Fragmentation by Blasting. Luleå University of Technology, Luleå, Sweden, pp 85–92

Conference paper II

Chi L, Aalberg A, Zhang ZX, et al (2018) An experimental investigation on dynamic responses of granite blocks under blast loading. In: Li C, Li X, Zhang Z (eds) Proceedings of the 3rd international conference on rock dynamic and applications. Taylor & Francis Group, Trondheim, pp 623–628

The conference papers are not included in NTNU Open due to copyright